



# Construction of rGO wrapping octahedral Ag-Cu<sub>2</sub>O heterostructure for enhanced visible light photocatalytic activity

Qi Wei<sup>a,\*</sup>, Yang Wang<sup>a,\*</sup>, Haiying Qin<sup>b,\*</sup>, Jinming Wu<sup>c</sup>, Yangfang Lu<sup>c</sup>, Hongzhong Chi<sup>b</sup>, Fan Yang<sup>a</sup>, Bin Zhou<sup>a</sup>, Houlin Yu<sup>a</sup>, Jiabin Liu<sup>c,\*</sup>

<sup>a</sup> Center for Optoelectronics Materials and Devices, Zhejiang Sci-Tech University, Hangzhou 310018, China

<sup>b</sup> College of Materials and Environmental Engineering, Hanzhou Dianzi University, Hangzhou 310018, China

<sup>c</sup> School of Materials Science and Engineering, Zhejiang University, Hangzhou 310027, China

## ARTICLE INFO

### Keywords:

Water bath method  
Heterostructure  
Visible light photocatalyst  
Cuprous oxide

## ABSTRACT

A ternary reduced graphene oxide wrapped octahedral Ag-Cu<sub>2</sub>O (Ag-Cu<sub>2</sub>O/rGO) photocatalyst has been synthesized through a facile one-pot water bath method at 55 °C. The ternary Ag-Cu<sub>2</sub>O/rGO composites possessed a novel heterostructure, in which Cu<sub>2</sub>O octahedra were decorated with dense Ag nanoparticles and were wrapped with thin rGO nanosheets. The ternary Ag-Cu<sub>2</sub>O/rGO photocatalyst exhibited much higher activity in photo-degradations of phenol in water under visible light than either pure Cu<sub>2</sub>O or binary Cu<sub>2</sub>O/rGO or Ag-Cu<sub>2</sub>O composites. The photo-excited electrons from Cu<sub>2</sub>O transferred to rGO and Ag, leading to the separation of the electron-hole pairs. The incorporation of rGO not only suppressed the recombination of electron-hole pairs but also prevented the agglomeration of Ag nanoparticles. Ag nanoparticles played an important role in the photocatalysis owing to the surface plasmon resonance.

## 1. Introduction

In recent years, semiconductor photocatalysts have received extensive attention due to the ability to solve the current energy and environmental problems with sustainable solar energy [1]. The photocatalytic process of semiconductor photocatalysts depends on the absorption of the solar spectrum and the separation of the photo-excited carriers. The low optical absorption efficiency in the visible region and the high recombination rate limit the practical applications of many semiconductor materials [2,3]. The most widely used photocatalysts are TiO<sub>2</sub> and ZnO, which only absorb ultraviolet light owing to their large band-gap. In order to practically harvest energy from sunlight, new photocatalysts working in the visible region are strongly required [4].

Cuprous oxide (Cu<sub>2</sub>O), a common p-type semiconductor with a narrow band gap of 2.0–2.2 eV, has been used in the field of photocatalysis and sensor due to its strong visible light response. Many kinds of Cu<sub>2</sub>O nanostructures such as cubes [5], octahedral [6] and 26-facet polyhedral [7], were successfully prepared and applied to the degradation of organic pollutants. It is found that Cu<sub>2</sub>O has a high recombination rate of photo-excited carriers, which leads to low quantum efficiency. Generally, it is believed that the binary Cu<sub>2</sub>O/noble metal (Au, Ag and Pt etc.) and Cu<sub>2</sub>O/reduced graphene oxide (rGO) heterostructure can effectively promote the separation and transfer of photo-

excited carriers. A large number of binary Cu<sub>2</sub>O/noble metal and Cu<sub>2</sub>O/rGO composites have been prepared and achieved improved photocatalytic performance [8]. However, there are still many fundamental problems for the application of the binary composite photocatalysts. For example, the agglomeration of the noble metal nanoparticles on the surface of Cu<sub>2</sub>O significantly deteriorates the performance and reusability of the catalyst. Compared with the binary Cu<sub>2</sub>O/noble metal and Cu<sub>2</sub>O/rGO composites, ternary noble metal-Cu<sub>2</sub>O/rGO composites may be more effective in improving the photocatalytic performance. This idea was carried out and was verified to be effective recently. Spherical Ag-Cu<sub>2</sub>O/rGO nanohybrids were prepared via a two-stage reduction synthetic route and achieved enhanced photocatalytic activity and recyclability [9]. More recently, Ag-Cu<sub>2</sub>O/GO nanocomposites were prepared by a ball milling-assisted solid-state reaction method and showed excellent photocatalytic activity towards methyl orange (MO) degradation [10]. It is well known that the surface plane of the Cu<sub>2</sub>O plays a key role in the photocatalysis, which is neglected in the previous ternary Ag-Cu<sub>2</sub>O/rGO nanocomposites. The octahedral Cu<sub>2</sub>O crystals with dominant {111} planes were confirmed to have super photocatalytic activity, because that the highly active {111} facets with unsaturated “Cu” had excellent activity on the dye degradation [11,12]. In this work, a novel ternary Ag-Cu<sub>2</sub>O/rGO heterostructure with regular Cu<sub>2</sub>O octahedral, dense Ag nanoparticles and rGO nanosheets was

\* Corresponding authors.

E-mail addresses: [wuyy2001@sina.com](mailto:wuyy2001@sina.com) (Y. Wang), [hyqin@hdu.edu.cn](mailto:hyqin@hdu.edu.cn) (H. Qin), [liujiabin@zju.edu.cn](mailto:liujiabin@zju.edu.cn) (J. Liu).

constructed through a facile one-pot water bath method at 55 °C. The resultant heterostructure exhibited excellent photocatalytic activity in degradation of phenol under visible light illumination.

## 2. Experiment

### 2.1. Raw materials

Natural graphite, sodium nitrate ( $\text{NaNO}_3$ ), potassium permanganate ( $\text{KMnO}_4$ ), hydrogen peroxide ( $\text{H}_2\text{O}_2$ ), concentrated sulfuric acid ( $\text{H}_2\text{SO}_4$ ), cupric chloride dehydrate ( $\text{CuCl}_2 \cdot 2\text{H}_2\text{O}$ ), polyvinylpyrrolidone (PVP K-30), ascorbic acid, sodium hydroxide ( $\text{NaOH}$ ), trisodium citrate dehydrate ( $\text{C}_6\text{H}_5\text{Na}_3\text{O}_7 \cdot 2\text{H}_2\text{O}$ ), disodium ethylenediaminetetraacetate ( $\text{Na}_2\text{-EDTA}$ ), *P*-benzoquinone (PBQ), isopropanol (IPA) and silver nitrate ( $\text{AgNO}_3$ ) were supplied by Sigma-Aldrich. All chemicals were of analytical grade and used without further purification. The deionized water used in the synthesis was obtained from Millipore Q purification system (resistivity > 18 M $\Omega$  cm).

### 2.2. Preparation of the octahedral Ag-Cu<sub>2</sub>O/rGO heterostructure

GO suspension was synthesized by chemical exfoliation of graphite powder under acidic conditions according to a modified Hummer's method [13]. Octahedral Ag-Cu<sub>2</sub>O/rGO heterostructure was prepared via a facile water bath method at 55 °C. In a typical synthesis, 8.8 g PVP, 0.1 g  $\text{C}_2\text{H}_5\text{Na}_3\text{O}_7 \cdot 2\text{H}_2\text{O}$  and 0.171 g  $\text{CuCl}_2 \cdot 2\text{H}_2\text{O}$  were dissolved into 100 mL GO aqueous solution. Subsequently, 10.0 mL NaOH aqueous solution (2 M) was added dropwise into the above solution. After stirring for 30 min, AA aqueous solution (10.0 mL, 0.6 M) was added dropwise to the above solution and stirred for 2.5 h. Finally, 20 mL of  $\text{AgNO}_3$  (5 mM) was added to the resultant solution and stirred for 30 min. All of these processes were performed in a water bath at 55 °C with vigorous magnetic stirring. The solid product was separated by centrifugation and washed repeatedly with distilled water and absolute alcohol to remove residual ions, and finally dried for 3 h in a vacuum oven at 70 °C for further characterization. The Ag-Cu<sub>2</sub>O/rGO composites with a different loading of Ag nanoparticles were prepared by controlling the concentration of  $\text{AgNO}_3$  (1, 2.5, 5 and 7.5 mM) under identical conditions. The resulting Ag-Cu<sub>2</sub>O/rGO samples were labeled as Ag<sub>1</sub>-Cu<sub>2</sub>O/rGO, Ag<sub>2.5</sub>-Cu<sub>2</sub>O/rGO, Ag<sub>5</sub>-Cu<sub>2</sub>O/rGO and Ag<sub>7.5</sub>-Cu<sub>2</sub>O/rGO, respectively.

For comparison, octahedral Cu<sub>2</sub>O was prepared without adding  $\text{AgNO}_3$  nor GO. Simultaneous, binary octahedral Ag-Cu<sub>2</sub>O and octahedral Cu<sub>2</sub>O/rGO composites were obtained by a similar procedure without adding GO or  $\text{AgNO}_3$ , respectively.

### 2.3. Characterization

The phase structure of the samples was analyzed by X-ray diffraction (XRD) using a German Bruker D8 diffractometer system with Cu K $\alpha$  ( $\lambda = 1.5406 \text{ \AA}$ ) radiation at 40 kV. Fourier transform infrared (FT-IR) spectra were characterized with a Nicolet Avatar 370 spectrometer. Raman spectra were recorded using a Bruker Raman microspectrometer. The microstructures and chemical composition were investigated by a scanning electron microscopy (SEM) on a Hitachi S4800 and a transmission electron microscopy (TEM) on a JEM-2100 equipped with energy dispersive spectrometers (EDS, Oxford). The X-ray photoelectron spectrometer (XPS), VB-XPS and ultraviolet photoelectron spectra (UPS) were measured using a Thermo Fisher Scientific Escalab250Xi system with monochromatic Al K $\alpha$  X-rays (1468.6 eV). The optical properties were studied through a Hitachi U-3900 UV-vis spectrophotometer and Hitachi F7000 PL fluorescence spectrophotometer at 325 nm. Total organic carbon (TOC) was tested on an Analytik Jean AG Multi N/C 2100 TOC analyzer. The intermediate products during the catalysis were tested on Agilent Technologies 7890A GC-MS analyzer.

The photocurrent-time curves were tested by the standard three-electrode configuration in a CHI660E electrochemical workstation. Platinum wire was used as the counter electrode, Ag/AgCl as the reference electrode, and samples as the working electrodes. For the working electrodes preparation, 10 mg photocatalyst powder was dispersed in a mixture of 5  $\mu\text{L}$  deionized water and 3  $\mu\text{L}$  absolute ethanol, followed by the addition of 2  $\mu\text{L}$  of Nafion reagent and sonication for 5 min to form a slurry. The slurry was uniformly coated on the FTO glass, the exposed electrode area was controlled to be 1 cm<sup>2</sup>. After air drying, the electrode was heating at 60 °C for 2 h to enhance adhesion. The  $\text{Na}_2\text{SO}_4$  (0.1 M) was used as the electrolyte. Electrochemical impedance spectra (EIS) was carried out in the same system with a frequency range from 0.01 Hz to 10 kHz at 5 mV. Mott-Schottky experiments were carried out at a frequency of 1000 Hz within the potential region of  $-0.6$  to  $0.6 \text{ V}$  vs Ag/AgCl reference electrode.

### 2.4. Photocatalysis experiments

The photocatalytic activities were evaluated by the photodegradation of phenol aqueous solution under the visible light illumination at room temperature. The photodegradation reactions were conducted in a quartz reactor equipped with a 300 W Xe lamp with a UV cut filter ( $\lambda > 420 \text{ nm}$ ). In a typical procedure, 50 mg photocatalyst was added into 50 mL phenol aqueous solution ( $10 \text{ mg L}^{-1}$ ). Before light illumination, the mixture was magnetically stirred in the dark for 30 min for attaining an adsorption-desorption equilibrium. During illumination, circulating water was used to ensure the temperature of the suspension at about 25 °C. At various time intervals, 3 mL suspension was taken, centrifuged and analyzed with a Hitachi U-3900 spectrophotometer to test the concentration of phenol.

## 3. Results and discussions

### 3.1. Microstructure characterizations

Fig. 1 shows the XRD patterns of the GO, Cu<sub>2</sub>O, Cu<sub>2</sub>O/rGO, Ag-Cu<sub>2</sub>O and Ag-Cu<sub>2</sub>O/rGO. For the GO, a sharp diffraction peak at 12.4° is detected, which matches the characteristic peak of the GO (001) plane. For the Cu<sub>2</sub>O, five primary diffraction peaks are indexed at 29.7°, 36.6°, 42.5°, 61.6° and 73.7°, which are attributed to the (110), (111), (200), (220) and (311) planes of the cubic phase Cu<sub>2</sub>O (JCPDS No.05-0667) [14,15]. No characteristic peak of CuO or Cu is observed. The XRD pattern of the Cu<sub>2</sub>O/rGO only shows the diffraction peaks matching with the Cu<sub>2</sub>O without obvious diffraction peak of the rGO. The reason is that regular layered structure of graphene sheets is destroyed after recombination with the Cu<sub>2</sub>O and the content of the rGO is much lower than the Cu<sub>2</sub>O [16]. For the Ag-Cu<sub>2</sub>O and Ag-Cu<sub>2</sub>O/rGO, besides the

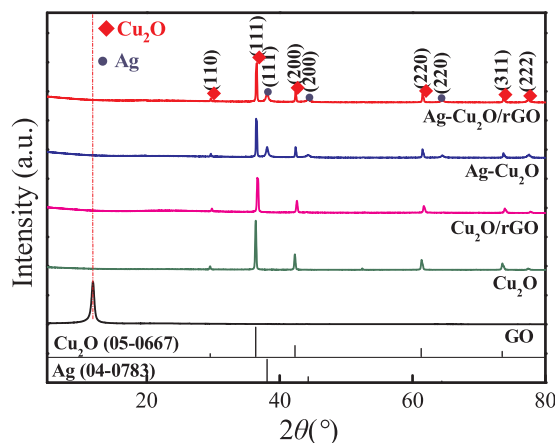


Fig. 1. XRD patterns of the GO, Cu<sub>2</sub>O, Cu<sub>2</sub>O/rGO, Ag-Cu<sub>2</sub>O and Ag-Cu<sub>2</sub>O/rGO.

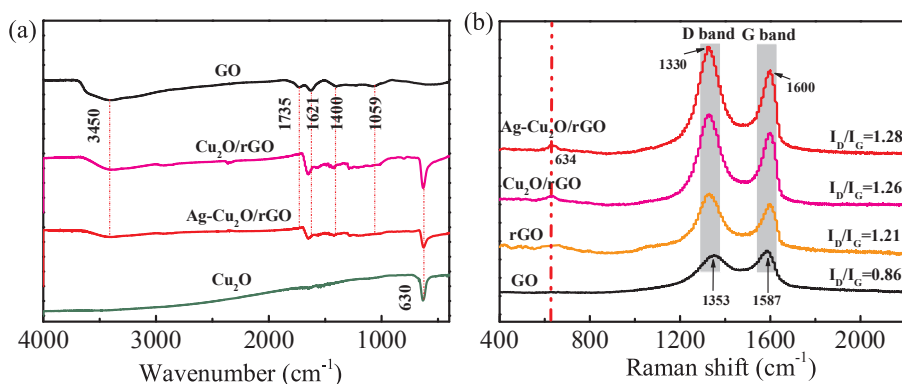


Fig. 2. (a) FT-IR and (b) Raman spectra of GO, rGO, Cu<sub>2</sub>O, Cu<sub>2</sub>O/rGO and Ag-Cu<sub>2</sub>O/rGO.

peaks of the Cu<sub>2</sub>O, characteristic peaks of Ag are also detected at 38.1°, 44.3° and 64.4°, which corresponds to the Ag (JCPDS No.04-0783) (111), (200) and (220) planes. This result confirms the existence of Ag in the Ag-Cu<sub>2</sub>O and Ag-Cu<sub>2</sub>O/rGO.

The effective reduction of GO into rGO can be verified via the FT-IR and Raman spectra. Fig. 2(a) shows the FT-IR spectra of the GO, Cu<sub>2</sub>O, Cu<sub>2</sub>O/rGO and Ag-Cu<sub>2</sub>O/rGO. For pure Cu<sub>2</sub>O, a typical absorption band at 630 cm<sup>-1</sup> is assigned to the stretching vibration of the Cu–O [8]. The absorption peaks of the GO at 3450, 1735, 1400 and 1059 cm<sup>-1</sup> are assigned to the stretching vibrations of the O–H groups, the carbonyl C=O, C–OH and alkoxy C–O, respectively [17]. In addition, the band at the 1621 cm<sup>-1</sup> is corresponding to the skeletal vibrations of graphitic domains [18]. After GO is reduced by AA, the bands for oxygen-containing groups (3450, 1735, 1621, 1400 and 1059 cm<sup>-1</sup>) are weakened or even disappear, suggesting the elimination of the oxygentic groups. Compared to the GO, the relative absorption peaks intensity of those oxygen-containing groups decrease notably in the spectra of the Cu<sub>2</sub>O/rGO and Ag-Cu<sub>2</sub>O/rGO, confirming the reduction of GO to rGO. Fig. 2(b) shows the Raman spectroscopy of the GO, Cu<sub>2</sub>O, Cu<sub>2</sub>O/rGO and Ag-Cu<sub>2</sub>O/rGO. Two peaks located at 1300–1650 cm<sup>-1</sup> are detected, which are the characteristic peaks of carbon materials: D and G peaks [19]. The D peak is attributed to the edge and sp<sup>3</sup> defects carbon, while the G peak belongs to the ordered vibrational sp<sup>2</sup> bonded carbon atoms [20]. Therefore, the defect density could be compared by relative peak intensity ratio of D peak to G peak ( $I_D/I_G$ ). The intensity ratios ( $I_D/I_G$ ) in the rGO (1.21), Cu<sub>2</sub>O/rGO (1.26) and Ag-Cu<sub>2</sub>O/rGO (1.28) are obviously higher than that in the GO (0.86), suggesting the formation of more sp<sup>3</sup> defects. For Cu<sub>2</sub>O/rGO and Ag-Cu<sub>2</sub>O/rGO, the additional peak at 634 cm<sup>-1</sup> belongs to the Cu<sub>2</sub>O.

In order to further confirm the successful reduction of AgNO<sub>3</sub> and GO, Ag-Cu<sub>2</sub>O/rGO was characterized by XPS measurement and the results are shown in Figs. S1 and 3. The peaks situated at 284.8, 367.9, 531.0 and 932.6 eV are attributed to C 1s, Ag 3d, O 1s and Cu 2p, respectively [21,22]. This result confirms the existence of rGO, Ag and Cu<sub>2</sub>O in the Ag-Cu<sub>2</sub>O/rGO composites. In the C 1s XPS spectrum of the GO (Fig. 3(a)), peaks at 284.6, 286.7 and 287.8 eV correspond to binding energies of C–C, C–O and C=O [23,24]. In the C 1s spectrum of Ag-Cu<sub>2</sub>O/rGO (Fig. 3(b)), only two peaks at around 284.6 and 286.7 eV are observed. The absence of C=O peak as well as the significant decrease of C–O peak in the Ag-Cu<sub>2</sub>O/rGO are mainly attributed to the reduction of GO to rGO. This result is in good agreement with the FT-IR and Raman results. The XPS pattern of Cu 2p is shown in Fig. 3(c). It can be clearly seen that the binding energies at 932.4 eV and 952.3 eV correspond to Cu 2p<sub>3/2</sub> and Cu 2p<sub>1/2</sub>, respectively, which are in good agreement with the data of Cu<sub>2</sub>O. For the Ag-Cu<sub>2</sub>O, these peaks are slightly shifted to 932.5 eV and 952.5 eV, respectively, owing to an interaction between the Cu<sub>2</sub>O and Ag. Meanwhile, it can be seen that the binding energies of Cu 2p in the Ag-Cu<sub>2</sub>O/rGO composites (932.8 and 952.7 eV) are slightly higher than those in the Ag-Cu<sub>2</sub>O, indicating that the rGO should interact with the Cu<sub>2</sub>O [25,26].

Unfortunately, it is difficult to distinguish the Cu<sup>+</sup> and Cu<sup>0</sup> in the Cu 2p<sub>3/2</sub> from the XPS spectrum due to the overlap of binding energy [27,28]. However, the AES pattern is an effective way to distinguish states between Cu<sup>+</sup> and Cu<sup>0</sup>. Fig. 3(d) and (e) shows the AES results of the pure Cu<sub>2</sub>O and the Ag-Cu<sub>2</sub>O/rGO. According to the literatures [29,30], the main peaks of the Cu LMM kinetic energies of Cu<sub>2</sub>O at 917.6 eV and 918.4 eV demonstrated the presence of Cu<sup>+</sup> and Cu<sup>0</sup>, respectively. In Fig. 3(d) and (e), only an obvious peak at 917.6 eV was detected. This result confirms presence of Cu<sup>+</sup> instead of metal Cu inside the Cu<sub>2</sub>O. As can be seen from Fig. 3(f), the peaks of Ag 3d<sub>5/2</sub> and Ag 3d<sub>3/2</sub> with binding energies of 367.8 and 373.8 eV in the Ag-Cu<sub>2</sub>O/rGO composites, respectively. The spin energy separation of the Ag 3d is 6.0 eV which is consistent with the standard spin energy separation of metallic Ag, confirming the existence of metallic Ag in the Ag-Cu<sub>2</sub>O/rGO [31]. Further comparison with the standard values of the Ag 3d<sub>5/2</sub> and Ag 3d<sub>3/2</sub> (368.2 and 374.2 eV) [32], the binding energies of the Ag 3d<sub>5/2</sub> and Ag 3d<sub>3/2</sub> in the Ag-Cu<sub>2</sub>O/rGO composites (367.8 and 373.8 eV) are slightly lower, which indicates an interaction between the Cu<sub>2</sub>O and Ag nanoparticles [33].

The microstructures of the Cu<sub>2</sub>O, Cu<sub>2</sub>O/rGO and Ag-Cu<sub>2</sub>O composites are shown in Figs. 4 and S2. Octahedral Cu<sub>2</sub>O with four pairs of exposed (111) facets are obtained as shown in Fig. 4(a). The mean diameter of octahedral Cu<sub>2</sub>O is measured to be 1.2 μm, and the mean edge length is 880 nm. The surface of the Cu<sub>2</sub>O is smooth and clean. The Cu<sub>2</sub>O/rGO composite is obtained by introducing rGO nanosheets as shown in Figs. 4(b) and S2(b). The rGO nanosheets exhibit a typical thin, transparent and wrinkle structure, and wrap onto the Cu<sub>2</sub>O. Fig. 4(c) and (d) is the SEM images of the Ag-Cu<sub>2</sub>O composite. The red circle in Fig. 4(c) is amplified and shown as Fig. 4(d). Compared to Fig. 4(a), the Cu<sub>2</sub>O surface is neither smooth nor clean but is deposited with dense Ag nanoparticles. The presence of the Ag nanoparticles is verified by the EDS results (Fig. 4(e) and (f)). Strong Ag peaks are identified in the EDS spectrum of the nanoparticle (site 1 in Fig. 4(f)) while the Ag peaks are invisible in the spectrum of the matrix (site 2 in Fig. 4(f)). The mean diameter of the Ag nanoparticles measured by TEM is 12 nm.

Fig. 5(a) shows the typical SEM image of the Ag-Cu<sub>2</sub>O/rGO composite and Fig. 5(b) shows the enlarged portion of the red circle in Fig. 5(a). The octahedral Ag-Cu<sub>2</sub>O composite is wrapped by rGO nanosheets. The existence of Ag nanoparticles on the surface of Cu<sub>2</sub>O in the Ag-Cu<sub>2</sub>O/rGO composites is further confirmed by the high resolution TEM image (Fig. 5(c)). The lattice intervals of rGO and Ag are 0.37 and 0.24 nm, which are in agreement with the (002) plane of rGO and (111) plane of Ag, respectively [34]. The above observations confirm that Ag nanoparticles have been successfully grown on the surface of the Cu<sub>2</sub>O crystal and the octahedral Ag-Cu<sub>2</sub>O is wrapped by rGO nanosheets in the ternary Ag-Cu<sub>2</sub>O/rGO composite. Based on the analysis of XRD, FTIR, Raman spectra, XPS, SEM, EDS-mapping (Fig. S3) and TEM, it is concluded that the ternary Ag-Cu<sub>2</sub>O/rGO composite has been successfully synthesized. The Ag content in the Ag-Cu<sub>2</sub>O/rGO

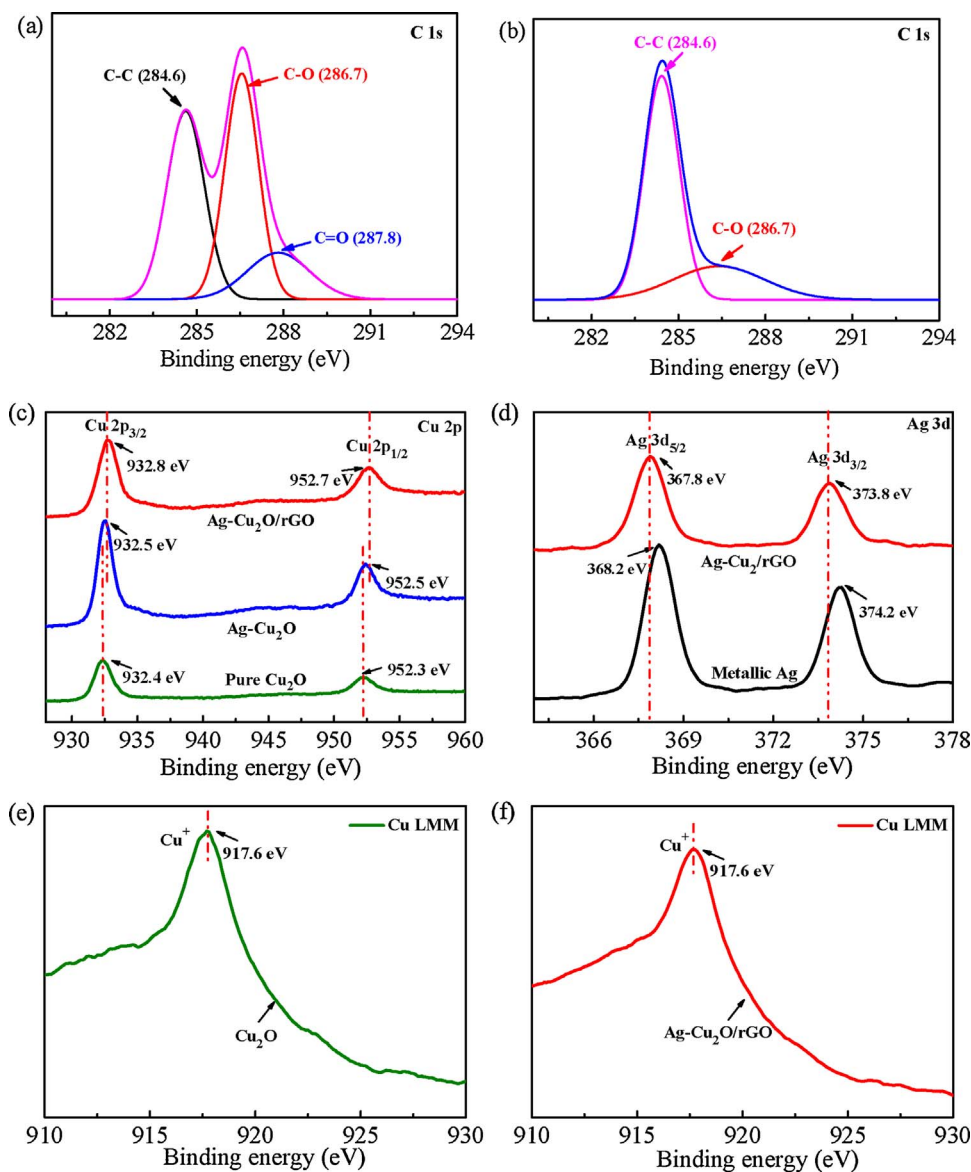


Fig. 3. (a) C1s XPS spectrum of GO. XPS spectra of (b) C 1s, (c) Cu 2p and (d) Ag 3d of Ag-Cu<sub>2</sub>O/rGO composites. (e) and (f) AES pattern of the Cu<sub>2</sub>O and Ag-Cu<sub>2</sub>O/rGO composites, respectively.

composite is tested by the EDS in SEM. Six regions of interest with a size of  $5\ \mu\text{m} \times 5\ \mu\text{m}$  were analyzed. A typical result is given in Fig. S4. The average content of Ag was calculated to be  $\sim 3.4\ \text{wt.}\%$ , and the molar ratio of Ag and Cu<sub>2</sub>O was 9:200 according to the EDS results.

### 3.2. Formation mechanism of the Ag-Cu<sub>2</sub>O/rGO

Based on the above experimental results, the formation process of the Ag-Cu<sub>2</sub>O/rGO heterostructure is schematically illustrated in Fig. 6. The evolution process mainly contains two stages: (1) the formation process of octahedral Cu<sub>2</sub>O/rGO; (2) the formation process of octahedral Ag-Cu<sub>2</sub>O on rGO sheet. First, when CuCl<sub>2</sub> was dissolved in the GO aqueous solution, the positively charged Cu<sup>2+</sup> was adsorbed on the GO surface due to the electrostatic adsorption action. Secondly, when excess NaOH solution was added, Cu<sup>2+</sup> and OH<sup>-</sup> formed Cu(OH)<sub>4</sub><sup>2-</sup> complex. Third, with the AA was added, Cu(OH)<sub>4</sub><sup>2-</sup> was reduced to Cu<sub>2</sub>O and GO was reduced to rGO. In this process, PVP played an important role in the shape control of Cu<sub>2</sub>O by selective face adsorption. The presence of PVP reduced the surface energy of {111} planes, which led to a shrinkage of {100} planes and an enlargement of the {111} planes to produce octahedral Cu<sub>2</sub>O, and deposit on the rGO to form Cu<sub>2</sub>O/rGO. In the second stage, Ag NPs were then deposited on the

Cu<sub>2</sub>O resulting in the formation of the Ag-Cu<sub>2</sub>O/rGO heterostructure. Although the Cu<sub>2</sub>O/rGO composite was formed before the Ag, Ag particles were able to deposit on the octahedral Cu<sub>2</sub>O due to following two factors: (1) The mixture of the Cu<sub>2</sub>O and rGO was mainly combined by van der Waals force instead of atomic bonding. So it was possible to have some “gap” between the Cu<sub>2</sub>O octahedra and rGO nanosheets. This situation may be frequent in a stirred environment during the synthesis process. As a result, AgNO<sub>3</sub> solution had chance to diffuse into the “gap”. (2) Huang et al. and Zhang et al. have predicted that Cu<sub>2</sub>O with {111} facets were thermodynamically favourable for the exchange of surface atoms with silver atoms [11,35]. So the Ag embryos preferred depositing on the surface of Cu<sub>2</sub>O instead of rGO.

### 3.3. Optical absorption properties

UV–vis diffuse reflectance spectroscopy (UV–DRS) spectra of the Cu<sub>2</sub>O, Cu<sub>2</sub>O/rGO, Ag-Cu<sub>2</sub>O and Ag-Cu<sub>2</sub>O/rGO composites are shown in Fig. 7(a). The pure Cu<sub>2</sub>O shows an absorption edge at 650 nm which belongs to the narrow-band-gap semiconductor Cu<sub>2</sub>O. The optical absorption edge shows a red-shift for the Cu<sub>2</sub>O/rGO, Ag-Cu<sub>2</sub>O and Ag-Cu<sub>2</sub>O/rGO composites compared to the pure Cu<sub>2</sub>O. The plot of  $(ah\nu)^2 - h\nu$  relationship curve was constructed to study the band gaps



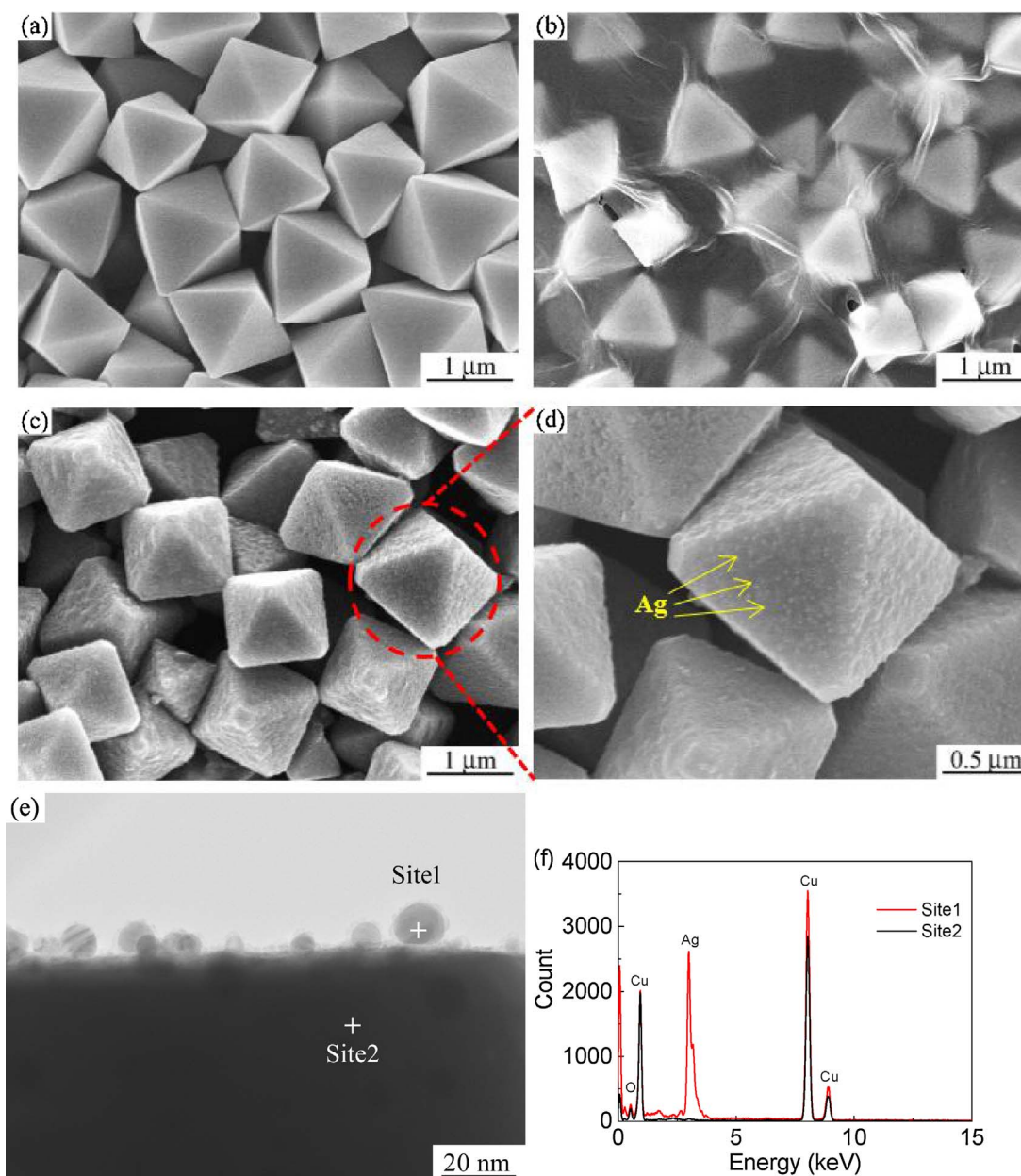


Fig. 4. SEM images of (a)  $\text{Cu}_2\text{O}$ , (b)  $\text{Cu}_2\text{O}/\text{rGO}$  and (c and d)  $\text{Ag-Cu}_2\text{O}$ , (e) TEM image of the  $\text{Ag-Cu}_2\text{O}$  and (f) EDS spectra corresponding to the site 1 and site 2 in (e).

and is shown in Fig. 7(b), where  $\alpha$  is absorption coefficient,  $h$  is Planck constant and  $\nu$  is the frequency. The band gaps of the pure  $\text{Cu}_2\text{O}$ ,  $\text{Cu}_2\text{O}/\text{rGO}$ ,  $\text{Ag-Cu}_2\text{O}$  and  $\text{Ag-Cu}_2\text{O}/\text{rGO}$  composites are 2.00, 1.90, 1.84 and 1.60 eV, respectively. The ordinal decrease of the band gap from pure  $\text{Cu}_2\text{O}$  to ternary composite is mainly due to that the strong interaction between the chemical bonds of each component promotes the electronic transfer across phase interface. In general, the  $\text{Ag-Cu}_2\text{O}/\text{rGO}$  composite has better optical absorption properties and narrower band gap than the other three. The reason may be attributed to the formation of Schottky barrier between Ag and  $\text{Cu}_2\text{O}$  and the surface plasmon resonance (SPR) effect [36,37]. The SPR effect of Ag in the composite could be confirmed by the absorption difference between  $\text{Cu}_2\text{O}/\text{rGO}$  and  $\text{Ag-Cu}_2\text{O}/\text{rGO}$ . As shown in Fig. S5, the UV-DRS absorbance spectra of  $\text{Cu}_2\text{O}/\text{rGO}$  and  $\text{Ag-Cu}_2\text{O}/\text{rGO}$  in the range of 450–550 nm are enlarged. It is obvious that there is an absorbance peak around the 500 nm in the spectrum of the  $\text{Ag-Cu}_2\text{O}/\text{rGO}$  while no obvious peak is found for the  $\text{Cu}_2\text{O}/\text{rGO}$ . The presence of the absorbance peak of the  $\text{Ag-Cu}_2\text{O}/\text{rGO}$  should be resulted from the introduction of Ag into the  $\text{Cu}_2\text{O}/\text{rGO}$ .

Previous studies demonstrate that the absorbance peak at around 500 nm is mainly attributed to the SPR effect of Ag [38].

### 3.4. Photocatalytic performance under visible light

Phenol, a typical colorless and persistent organic industrial waste, which involves no photosensitization procedure during the photocatalytic reaction, was employed to perform degradation experiments. As shown in Fig. S6, the results of dark absorption of the  $\text{Ag-Cu}_2\text{O}/\text{rGO}$  and direct photodegradation experiment manifest that the dark adsorption and self-sensitization of phenol in the reaction system are negligible. For pure  $\text{Cu}_2\text{O}$ , the degradation efficiency of phenol is only 40.7% for a degradation time of 210 min, respectively (Fig. 8(a)). The binary composites containing  $\text{Cu}_2\text{O}/\text{rGO}$  and  $\text{Ag-Cu}_2\text{O}$  exhibit higher catalytic activity, and the degradation efficiencies of phenol are increased to 60.5% and 78.8%. The results indicate that the introduction of Ag nanoparticles or rGO nanosheets could promote the photocatalytic performance of binary composites. Compared with single-

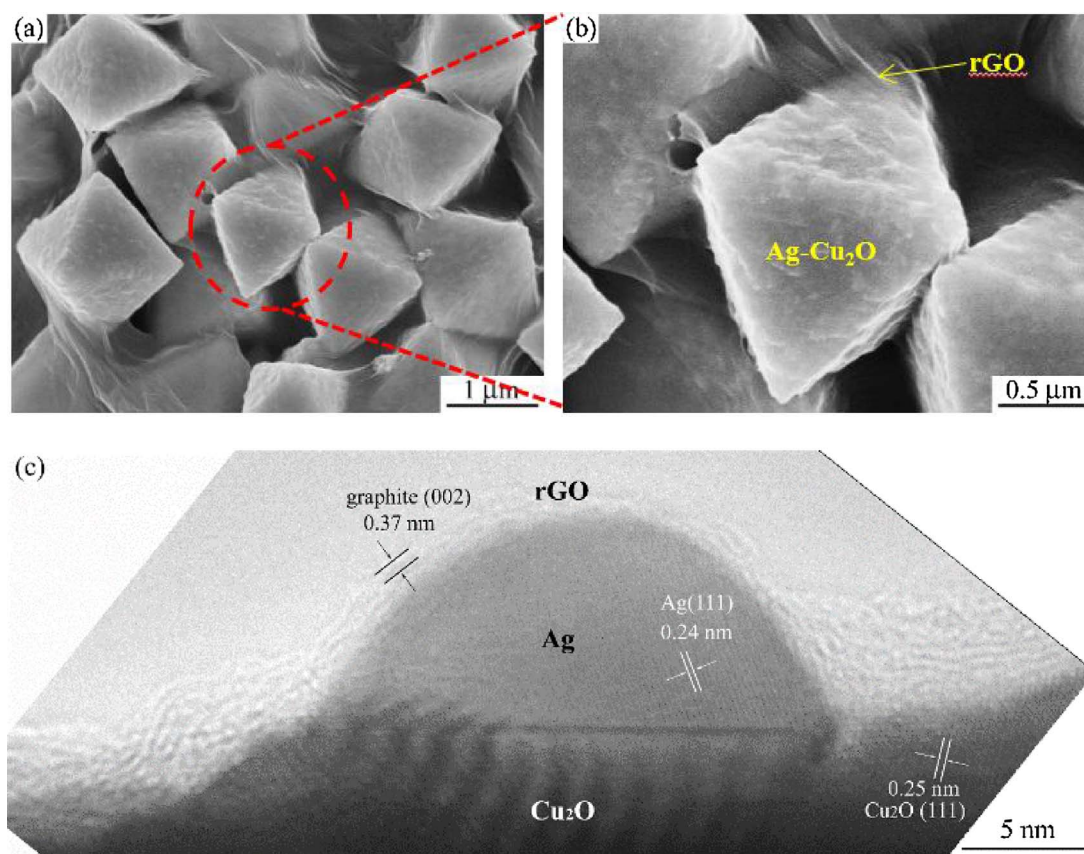


Fig. 5. (a and b) SEM images and (c) high resolution TEM image of the Ag-Cu<sub>2</sub>O/rGO composite.

component and binary catalysts, the ternary Ag-Cu<sub>2</sub>O/rGO heterostructures exhibit excellent photocatalytic activity towards phenol and the degradation efficiency of phenol is increased to 96.8%. It is noteworthy that the degradation of phenol is expected to follow a pseudo-first-order kinetics reaction. As shown in Fig. 8(b), the photodegradation rate constant of Ag-Cu<sub>2</sub>O/rGO is determined to be 0.0140 min<sup>-1</sup>, which is 2.1, 3.4 and 6.1 times than those of Ag-Cu<sub>2</sub>O (0.0066 min<sup>-1</sup>), Cu<sub>2</sub>O/rGO (0.0041 min<sup>-1</sup>) and Cu<sub>2</sub>O (0.0023 min<sup>-1</sup>), respectively. Therefore, the photocatalytic activity of the four samples follows the order of Ag-Cu<sub>2</sub>O/rGO > Ag-Cu<sub>2</sub>O > Cu<sub>2</sub>O/rGO > Cu<sub>2</sub>O. In order to further study the effect of Ag content on photocatalytic activity in the

compound, the degradation curves of phenol by Ag-Cu<sub>2</sub>O/rGO composites with different concentration of AgNO<sub>3</sub> (1 mM, 2.5 mM, 5 mM and 7.5 mM,) are given in Fig. 8(c). Photocatalytic activity is strongly dependent on the content of Ag in the composites. Either a low content or a high content of Ag results in relatively low photodegradation efficiency. So it is clearly that there is a suitable dosage of AgNO<sub>3</sub> (5 mM in this work) for Ag-Cu<sub>2</sub>O/rGO to achieve optimized photocatalytic activity. Similar optimum Ag loading for Cu<sub>2</sub>O/rGO was also found in previous work [39]. As reported in the literature, Ag nanoparticles dispersed on the surface of the Cu<sub>2</sub>O act as electron sinks to promote the separation of photoexcited electron and hole, so as to enhance

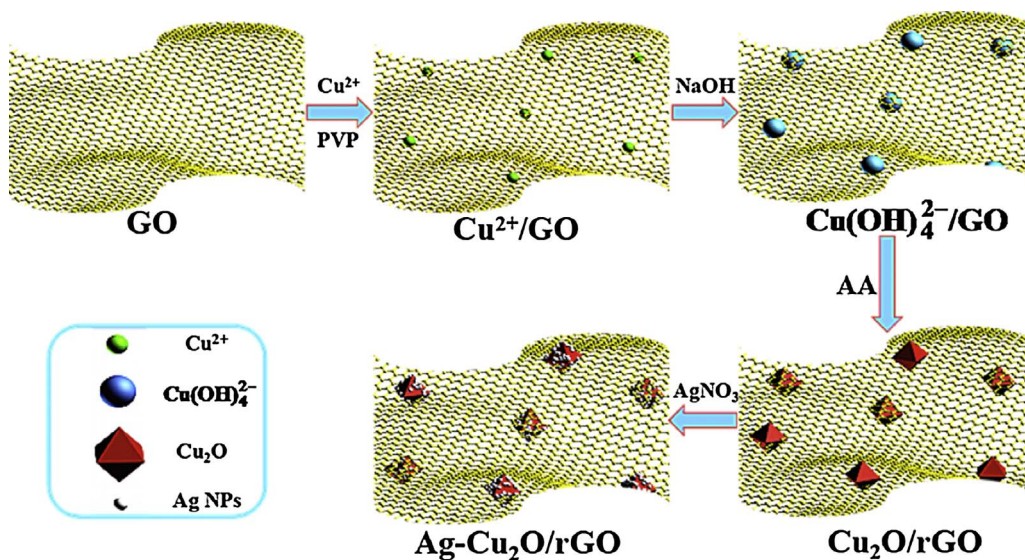


Fig. 6. Schematic illustration of synthesis of the Ag-Cu<sub>2</sub>O/rGO composite.

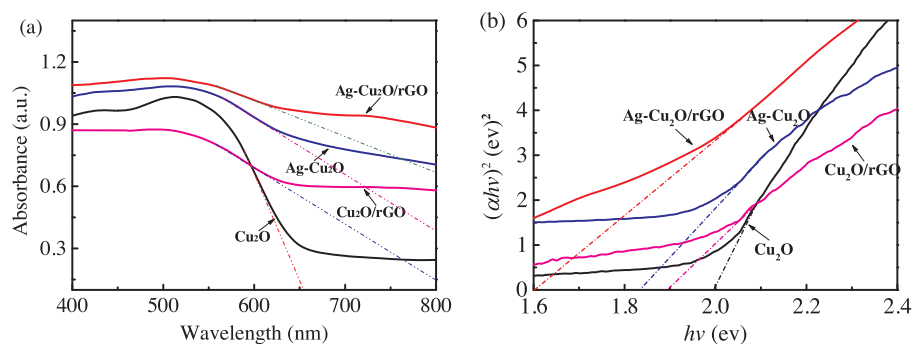


Fig. 7. (a) UV-DRS absorbance spectra and (b) plots of  $(\alpha h\nu)^2$  vs  $(h\nu)$  for the Cu<sub>2</sub>O, Cu<sub>2</sub>O/rGO, Ag-Cu<sub>2</sub>O and Ag-Cu<sub>2</sub>O/rGO composites.

photocatalytic activity. Unfortunately, a relatively high concentration of AgNO<sub>3</sub> may cause excessive Ag nanoparticles as new recombination centers for electron-hole, resulting in low photocatalytic efficiency [20,40].

The main derivatives produced in the process of photocatalytic degradation of phenol were shown in Fig. 9(a). These intermediate products mainly include *p*-benzoquinone, catechol and hydroquinone, which belong to aromatic intermediates. As the irradiation time increases, the concentration of phenol decreases and the concentration of these intermediates reaches a maximum and then decreases gradually due to the ring cleavage process [41]. These intermediates are further oxidized and eventually mineralized into carbon dioxide and water. The possible pathways of phenol degradation under visible light irradiation are illustrated in Fig. S7. TOC is an important and necessary parameter for measuring phenol fully mineralized into CO<sub>2</sub> and H<sub>2</sub>O in the photocatalytic reaction system. The Ag-Cu<sub>2</sub>O/rGO is selected as a representative photocatalyst, and the evaluation results of TOC during light irradiation are shown in Fig. 9(b). In the case of Ag-Cu<sub>2</sub>O/rGO, 64.5% of TOC of phenol is removed after 6 h of photocatalysis respectively, revealing that Ag-Cu<sub>2</sub>O/rGO is an excellent visible light responsive photocatalyst capable of deep mineralization of organic pollutants.

The stability of the photocatalyst is another key issue for practical application besides the photocatalytic activity. To assess the stability of the catalyst, the cyclic experiments of the Ag-Cu<sub>2</sub>O, Cu<sub>2</sub>O/rGO and Ag-

Cu<sub>2</sub>O/rGO were performed to degrade phenol under visible light irradiation for four times (Fig. 10(a)). The Cu<sub>2</sub>O/rGO and Ag-Cu<sub>2</sub>O/rGO have slight reduction in the degradation efficiency after four consecutive cycles. However, the degradation efficiency of phenol was less than 32.9% after four cycles by the Ag-Cu<sub>2</sub>O. The photocatalysts after four cycles of photocatalysis tests was characterized by XRD and SEM as displayed in Fig. 10(b–e). Compared with the fresh sample, there is not significant change in the XRD spectra of Cu<sub>2</sub>O/rGO and Ag-Cu<sub>2</sub>O/rGO photocatalyst after four cycles. However, a new peak located at 38.7° appears in the Ag-Cu<sub>2</sub>O. This peak corresponds to the CuO, which means that part of the Cu<sub>2</sub>O would be oxidized to CuO during photocatalytic degradation. This phenomenon has also been widely observed in the reaction system of Cu<sub>2</sub>O by other researchers. To further investigate the morphology change of the photocatalyst, SEM images of the photocatalysts after four repeated experiments were conducted and the images were provided in Fig. 10(c–e). The results indicate that the morphology of Cu<sub>2</sub>O/rGO (Fig. 10(d)) and Ag-Cu<sub>2</sub>O/rGO (Fig. 10(e)) after the four recycle experiment are almost the same as that of the fresh samples. By contrast, the morphology of the Ag-Cu<sub>2</sub>O has been changed obviously. As displayed in Fig. 10(c), Ag nanoparticles fall-off from the surface of Cu<sub>2</sub>O and agglomerated. In addition, a large number of holes appeared on the Cu<sub>2</sub>O surface, which was attributed to the high photocorrosion in the photocatalytic process. Therefore, according to the results mentioned above, we can preliminary conclude that the photocatalytic stability is mainly dependent on the introduction of rGO.

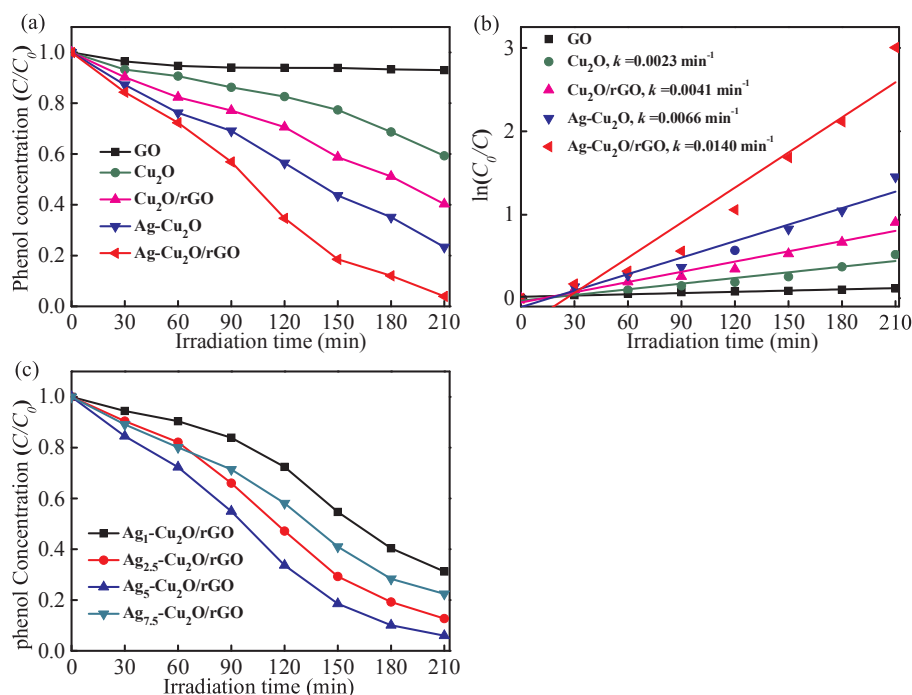


Fig. 8. (a) Photocatalytic activity and (b)  $\ln(C_0/C)$  vs.  $t$  plot for photodegradation of phenol by GO, Cu<sub>2</sub>O, Ag-Cu<sub>2</sub>O, Cu<sub>2</sub>O/rGO and Ag-Cu<sub>2</sub>O/rGO. (c) The phenol photodegradation for Ag-Cu<sub>2</sub>O/rGO photocatalyst with various dosage of AgNO<sub>3</sub>.



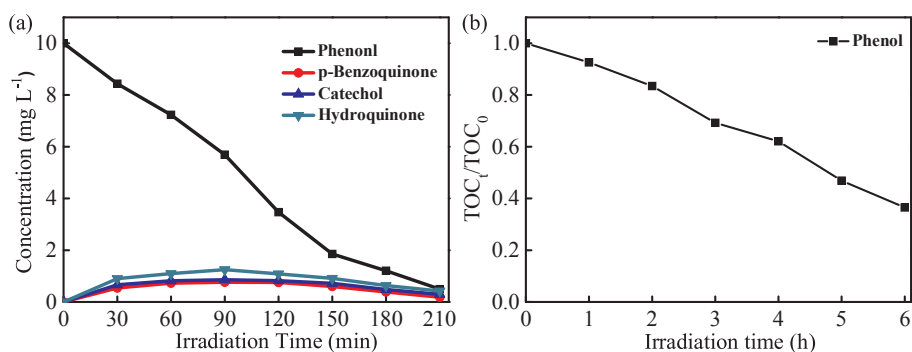


Fig. 9. (a) Distribution of the intermediates products and (b) TOC removals as a function of light irradiation time for the solution of phenol in the Ag-Cu<sub>2</sub>O/rGO photocatalysis system.

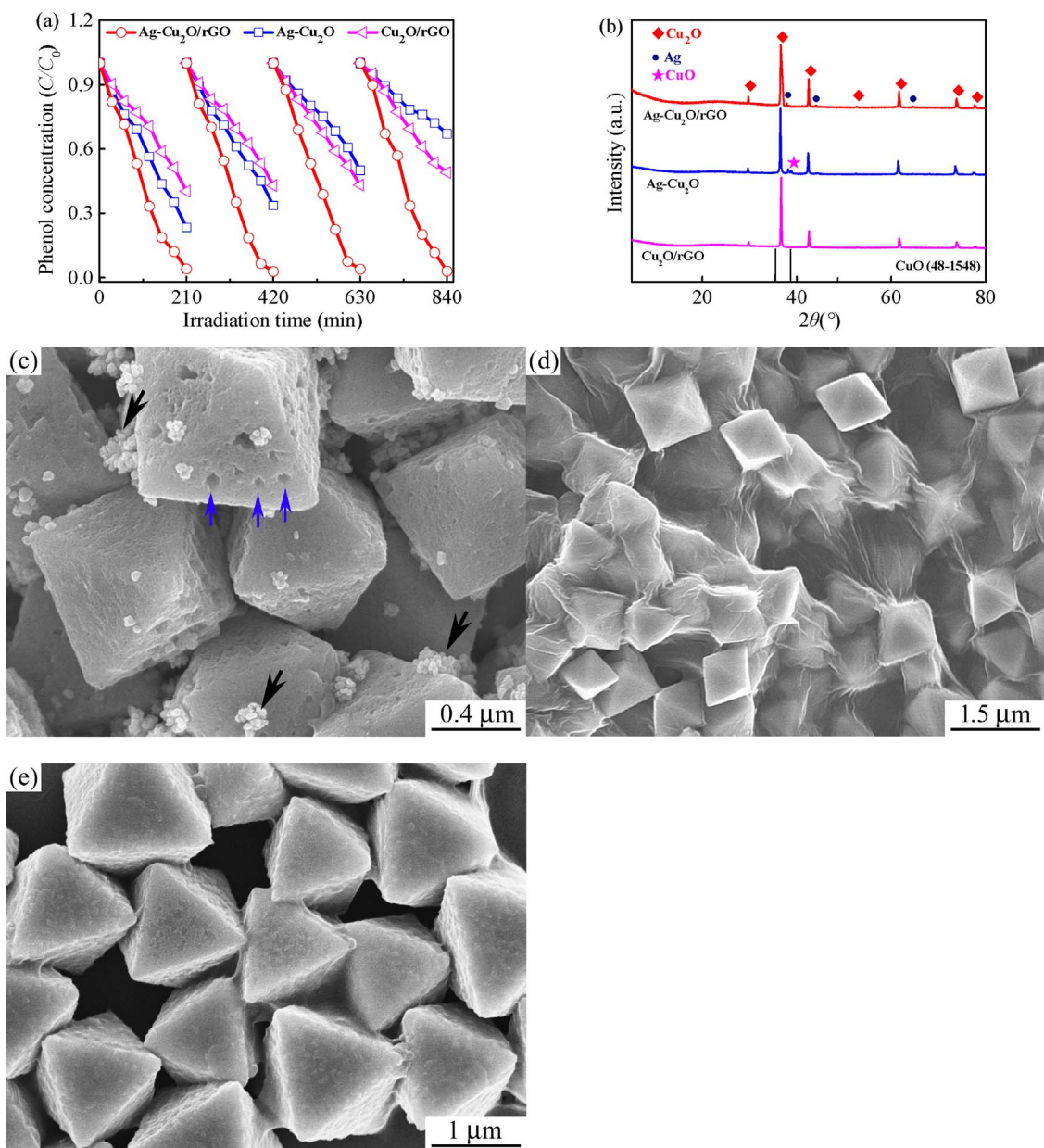


Fig. 10. (a) Cycling degradation of phenol by the Ag-Cu<sub>2</sub>O and Ag-Cu<sub>2</sub>O/rGO under visible light irradiation. (b) XRD pattern and (c) SEM image of the Ag-Cu<sub>2</sub>O/rGO after four-cycle photocatalysis tests.

The octahedral Ag-Cu<sub>2</sub>O composites are wrapped with rGO nanosheets, which can effectively protect the morphology and structure changes. Meanwhile, the presence of rGO nanosheets also inhibits agglomeration of Ag nanoparticles.

### 3.5. Mechanisms for improved photocatalytic activity

In the photocatalysis process, the effective separation and transfer of carriers are the most important factor for photocatalytic activity [42].



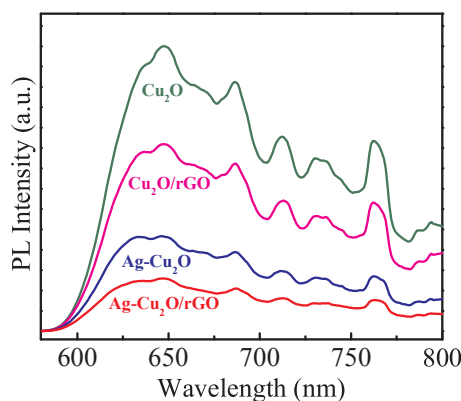


Fig. 11. PL spectra of the  $\text{Cu}_2\text{O}$ ,  $\text{Cu}_2\text{O}/\text{rGO}$ ,  $\text{Ag-Cu}_2\text{O}$  and  $\text{Ag-Cu}_2\text{O}/\text{rGO}$  composites.

PL test was carried out to study the  $\text{Cu}_2\text{O}$ ,  $\text{Cu}_2\text{O}/\text{rGO}$ ,  $\text{Ag-Cu}_2\text{O}$  and  $\text{Ag-Cu}_2\text{O}/\text{rGO}$  composites with an excitation wavelength of 325 nm, as shown in Fig. 11. With the introduction of rGO and Ag, the PL intensities of the composites are significantly lower than that of pure  $\text{Cu}_2\text{O}$ . The  $\text{Ag-Cu}_2\text{O}/\text{rGO}$  composite shows the lowest intensity than others at the same test conditions. In general, lower intensity suggests higher carrier separation rate and higher catalytic activity. The PL intensity sequence is consistent with the results of photocatalytic degradation. In the  $\text{Cu}_2\text{O}/\text{rGO}$ , the lower carrier recombination rate may be due to rGO excellent conductivity which allows photo-excited electrons to be efficiently transferred from the  $\text{Cu}_2\text{O}$  to rGO nanosheets [43]. In the  $\text{Ag-Cu}_2\text{O}$ , the lower carrier recombination rate may be due to the Schottky barrier formed at the metal-semiconductor interface which acts as an electron sink to prevent the electron-hole recombination. In the case of the  $\text{Ag-Cu}_2\text{O}/\text{rGO}$ , the lowest carrier recombination rate should benefit from the synergistic effects of the Ag and the rGO.

The nature of catalytic behavior of semiconductor photocatalyst is the process of photoelectric transformation. So the photoelectric conversion capability and carrier separation ability are usually evaluated by photoelectrochemical test. A remarkable observation come from a transient photocurrent response of the  $\text{Cu}_2\text{O}$ ,  $\text{Cu}_2\text{O}/\text{rGO}$ ,  $\text{Ag-Cu}_2\text{O}$  and  $\text{Ag-Cu}_2\text{O}/\text{rGO}$  composites during the visible light on-off irradiation cycles, as shown in Fig. 12(a). After four cycles of visible light switch on and off, the resulting photocurrents are still stable and renewable. Under visible light irradiation, the photocurrent density of  $\text{Ag-Cu}_2\text{O}/\text{rGO}$  ( $3.58 \times 10^{-4} \text{ mA cm}^{-2}$ ) is 1.44, 1.98 and 4.49 times higher than that of  $\text{Ag-Cu}_2\text{O}$  ( $2.47 \times 10^{-4} \text{ mA cm}^{-2}$ ),  $\text{Cu}_2\text{O}/\text{rGO}$  ( $1.81 \times 10^{-4} \text{ mA cm}^{-2}$ ) and  $\text{Cu}_2\text{O}$  ( $0.78 \times 10^{-4} \text{ mA cm}^{-2}$ ), respectively. These results illustrate that the photocarrier separation efficiency is higher in the  $\text{Ag-Cu}_2\text{O}/\text{rGO}$  composite than in other materials. As a result, it can be speculated that the introduction of Ag nanoparticles and rGO nanosheets accelerates the separation of photo-generated electron-hole pairs, which explains the enhanced photocatalytic activity of the composites.

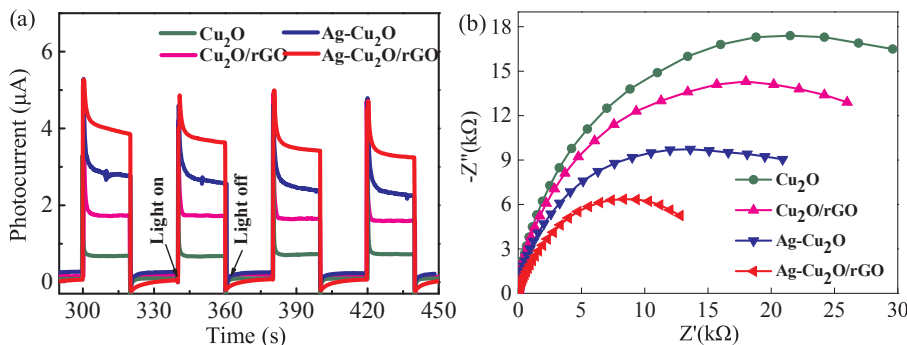


Fig. 12. (a) Transient photocurrent responses and (b) EIS of the  $\text{Cu}_2\text{O}$ ,  $\text{Cu}_2\text{O}/\text{rGO}$ ,  $\text{Ag-Cu}_2\text{O}$  and  $\text{Ag-Cu}_2\text{O}/\text{rGO}$  composites under visible light irradiation.

To validate the promoted carrier transfer behavior of the catalysts, the electrochemical impedance spectroscopy (EIS) of the different electrodes under visible-light irradiation ( $\lambda > 420$ ) is shown in Fig. 12(b). The radius of the circular arc at the high frequency region in the Nyquist curves reflects the separation efficiency of photogenerated carriers and the smaller radius of the circular arc implies more efficient separation efficiency of the electron-hole pairs [44,45]. From the Nyquist plots (Fig. 12(b)), the plots of all samples show a characteristic semicircle, which can be attributed to the space charge in a semiconductor [46]. More importantly, the semicircle of  $\text{Ag-Cu}_2\text{O}/\text{rGO}$  electrode under visible-light irradiation exhibits the smallest radius compared with the other electrodes, indicating that the separation of the photocarriers should be more effective and the interfacial charge transfer should be more rapid in the  $\text{Ag-Cu}_2\text{O}/\text{rGO}$  than other electrodes.

To investigate the predominant active species for phenol degradation in the photocatalytic reaction process and understand the reaction mechanism in depth, three different scavengers,  $\text{Na}_2\text{-EDTA}$ , PBQ and IPA were used for the investigation of the hole ( $\text{h}^+$ ), super oxide radical ( $\cdot\text{O}_2^-$ ) and hydroxyl radical ( $\cdot\text{OH}$ ), respectively. As shown in Fig. 13(a) and (b), after the addition of PBQ into the catalytic degradation process, the phenol degradation efficiency decreased from 93.4% to 19.1%, which indicated that the leading role of  $\cdot\text{O}_2^-$  in the catalytic process. Meanwhile, with the addition of  $\text{Na}_2\text{-EDTA}$ , the photocatalytic efficiency of  $\text{Ag-Cu}_2\text{O}/\text{rGO}$  was also inhibited greatly, indicating that the photogenerated  $\text{h}^+$  played a secondary role in the photocatalytic degradation. Moreover, the addition of IPA also resulted in the decreased degradation efficiency of phenol to some extent, suggesting the  $\cdot\text{OH}$  was also formed and took part in the photocatalytic degradation process. Since the photogenerated  $\text{h}^+$  in the valance band of  $\text{Cu}_2\text{O}$  ( $E_{\text{VB}} = +0.86 \text{ V}$ , vs NHE) were incapable of oxidizing hydroxyl groups into  $\cdot\text{OH}$  radicals ( $E(\cdot\text{OH}/\text{OH}^-) = +1.99 \text{ V}$ , vs NHE) due to the more negative valance band potential, it is believed that the  $\cdot\text{OH}$  radicals were generated from the  $\cdot\text{O}_2^-$  radicals by photochemical reaction [41,47]. According to the results mentioned above, we can preliminary conclude that in the  $\text{Ag-Cu}_2\text{O}/\text{rGO}$  degradation system,  $\cdot\text{O}_2^-$  and  $\text{h}^+$  species played major roles in phenol degradation in the photocatalytic degradation process. In addition, the  $\cdot\text{OH}$  species also participated in the catalytic reaction, contributing to the enhanced performance to some extent.

### 3.6. Photocatalytic mechanism based on energy band

VB-XPS spectroscopy, Mott-Schottky plots and their corresponding UV-DRS spectra were used to determine the potentials of VB (VB) and CB (CB) in  $\text{Cu}_2\text{O}$  before and after the Ag loading. The VB-XPS spectrum of the tested samples were calibrated by using the XPS profile of standard Ag as the benchmark. Fig. 14(a) and (b) shows the VB-XPS spectra of  $\text{Cu}_2\text{O}$  and  $\text{Ag-Cu}_2\text{O}$ , respectively. As can be seen from Fig. 14, the VB potential for  $\text{Cu}_2\text{O}$  is determined to be 0.86 eV vs NHE. For  $\text{Ag-Cu}_2\text{O}$ , the VB potential is 0.98 eV vs NHE, which is 0.12 eV more positive than  $\text{Cu}_2\text{O}$ .

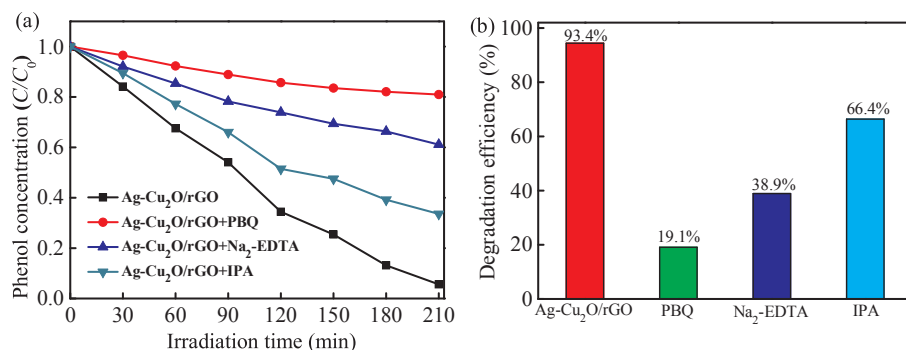


**Fig. 13.** (a) Trapping experiment for the photocatalytic degradation of phenol and (b) the corresponding photocatalytic removal efficiency over Ag-Cu<sub>2</sub>O/rGO composite under visible light irradiation.

To better understand and explain the band gap changes observed with Ag-Cu<sub>2</sub>O composites, the Mott-Schottky equation was further applied for studying the energy band of the pure Cu<sub>2</sub>O and Ag-Cu<sub>2</sub>O composites. The obtained Mott-Schottky plot is shown in Fig. 15. The negative slope in the linear region verified the *p*-type conductor of both pure Cu<sub>2</sub>O and Ag-Cu<sub>2</sub>O [48]. Flatband potentials were obtained by the calculation of the intersection of the line fit to the 1/C<sup>2</sup> measurements with the x-axis, which is 0.24 and 0.38 eV for pure Cu<sub>2</sub>O and Ag-Cu<sub>2</sub>O, respectively. Shifting of positive values of the flatband potential indicates the better ability of the composites to facilitate the charge separation in photocatalytic applications [49]. The flatband potentials could be equated to the VB edges for the *p*-type conductor [50]. Generally, the potential measured against an Ag/AgCl reference could be converted into normal hydrogen electrode potentials by using Eq. (1) [51]:

$$E_{\text{NHE}} = E_{\text{AgCl}} + E_{\text{AgCl}}^0 + 0.059 \text{ pH} \quad (1)$$

where  $E_{\text{AgCl}}^0 = 0.197 \text{ V}$  and the measured pH value of the electrolyte is approximately 7.0. Therefore, the calculated flatband position of pure Cu<sub>2</sub>O and Ag-Cu<sub>2</sub>O is 0.85 and 0.99 V vs NHE, respectively. Therefore, the corresponding VB of pure Cu<sub>2</sub>O and Ag-Cu<sub>2</sub>O found at 0.85 and 0.99 V vs NHE, respectively, which is consistent with the VB-XPS test results.

Combining the band gap results and the above VB values, the CB of the pure Cu<sub>2</sub>O and Ag-Cu<sub>2</sub>O can be calculated to be −1.14 and −0.86 eV vs NHE, respectively. On the basis of the relative VB and CB levels of Cu<sub>2</sub>O and Ag-Cu<sub>2</sub>O, a schematic of the energy band alignment for the composite can be obtained, as shown in Fig. 16. It can be seen that the  $E_{\text{CB}}$  of the Ag-Cu<sub>2</sub>O is by 0.28 eV more oxidizing than the  $E_{\text{CB}}$  of the pure Cu<sub>2</sub>O.

Ultraviolet photoelectron spectra (UPS) was adopted to test the work function and then the work function was used to determine the Fermi level. Fig. 17(a) shows the UPS spectra of the three relevant samples including pristine Ag nanoparticles, pure Cu<sub>2</sub>O and Ag-Cu<sub>2</sub>O. The excitation source was He I ( $h\nu = 21.22 \text{ eV}$ ) and a negative bias of −9.8 V was applied during the measurement. The photoemission

spectra were corrected to zero point as the Fermi level, which revealed the typical secondary-electron cut-off energy at 17.12, 16.81 and 16.92 eV for Ag nanoparticles, pure Cu<sub>2</sub>O and Ag-Cu<sub>2</sub>O, as shown in Fig. 17(b). This cut-off spectral feature describes that the excited electrons have lost much of their kinetic energy and no longer escape from the sample surface [52]. The difference between the photon energy and the cut-off energy therefore stands for the work function of the tested sample, giving 4.10, 4.41 and 4.30 eV for Ag nanoparticles, pure Cu<sub>2</sub>O and Ag-Cu<sub>2</sub>O, respectively. The corresponding energy of the Fermi level of Ag nanoparticles, pure Cu<sub>2</sub>O and Ag-Cu<sub>2</sub>O were estimated to be −4.10, −4.41 and −4.30 eV, respectively. On the other hand, the spectral distribution close to the Fermi level represents the VB structure of the tested sample. By performing linear extrapolation along the tangent of the spectrum onset the top of VB can be obtained. As displayed in Fig. 17(c), the top of VB of pure Cu<sub>2</sub>O and Ag-Cu<sub>2</sub>O were respectively computed as 0.90 and 1.11 eV. With the addition of the work function, the top of the VB with respect to the vacuum level can be determined as −5.31 and −5.41 eV for Cu<sub>2</sub>O and Ag-Cu<sub>2</sub>O, respectively. Considering the average bandgap energy value (2.0 eV for Cu<sub>2</sub>O and 1.84 eV for Ag-Cu<sub>2</sub>O) obtained from the UV-DRS spectra, the bottom of CB of the Cu<sub>2</sub>O and Ag-Cu<sub>2</sub>O with respect to vacuum level were calculated to be −3.31 eV and −3.57 eV, respectively. Combining these results, we delineated the band structure of Ag-Cu<sub>2</sub>O in Fig. 18 and proposed a charge transfer model to specify the prevalence of significant charge separation. First, Ag nanoparticles form a metal-semiconductor heterostructure with the Cu<sub>2</sub>O matrix. Since the work function of Ag (4.10 eV) is lower than that of the Cu<sub>2</sub>O (4.41 eV), the electrons are transferred from Ag to Cu<sub>2</sub>O until the new thermodynamic equilibrium is established, as shown in Fig. 18(a). This will move up the Fermi level of the Cu<sub>2</sub>O and down shift the Fermi energy of Ag as labelled as new  $E_{\text{F}} = 4.30 \text{ eV}$  in Fig. 18(b). When the sample is irradiated with visible light, the photo-excited electrons can transfer from the CB of the Cu<sub>2</sub>O to the surface of Ag nanoparticles because the CB of Cu<sub>2</sub>O is higher than the new Fermi level. On the one hand, the Ag nanoparticles act as an electron trap to suppress the recombination of  $e^-$  and  $h^+$  because of the Schottky barrier formed between the Ag and the Cu<sub>2</sub>O

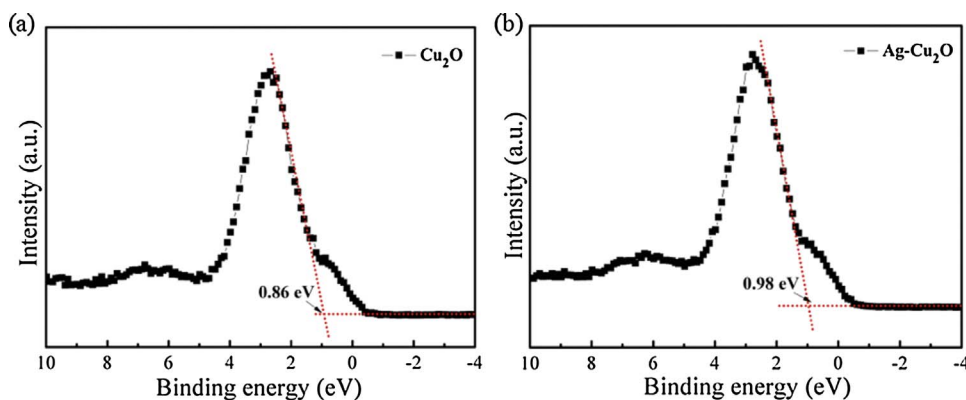


**Fig. 14.** VB-XPS spectra of (a) Cu<sub>2</sub>O and (b) Ag-Cu<sub>2</sub>O.

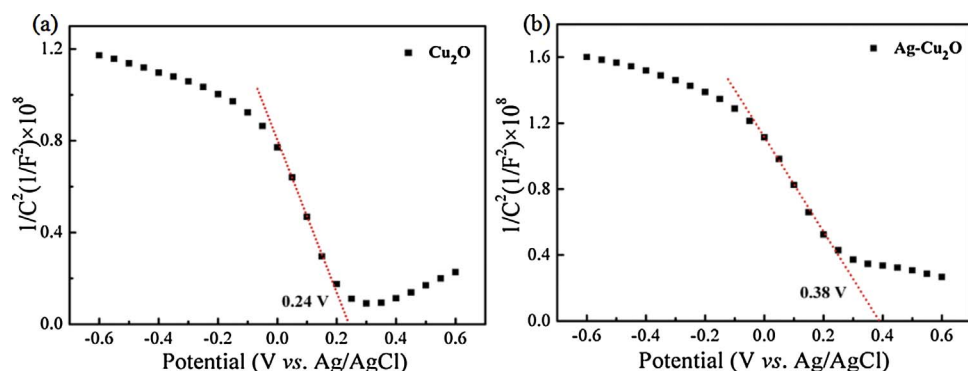


Fig. 15. Mott-Schottky plots for (a) pure  $\text{Cu}_2\text{O}$  and (b)  $\text{Ag-Cu}_2\text{O}$  composites coated onto FTO glass in 0.2 M  $\text{Na}_2\text{SO}_4$  electrolyte (pH = 7)  $\text{Cu}_2\text{O}$  and  $\text{Ag-Cu}_2\text{O}$ .

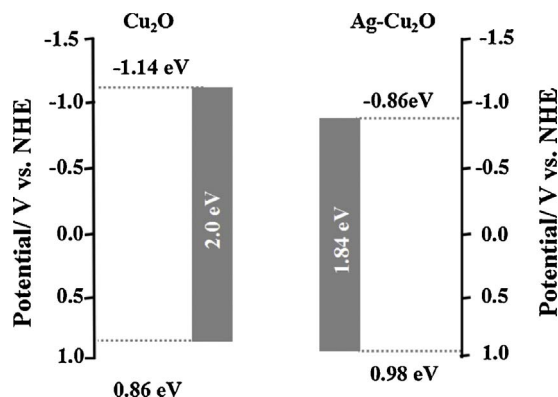


Fig. 16. Schematic diagram of band structure for  $\text{Cu}_2\text{O}$  and  $\text{Ag-Cu}_2\text{O}$ .

metal-semiconductor interface [53]. Therefore, this vectorial charge transfer resulted in spatial separation of charge carriers for  $\text{Cu}_2\text{O}$ , which was beneficial to the enhancement of the photocatalytic performance. On the other hand, since the Fermi level of rGO ( $-4.42$  eV) [54,55] is below the potential of the CB of  $\text{Cu}_2\text{O}$  in the  $\text{Ag-Cu}_2\text{O/rGO}$  composite, the photo-excited electrons on the CB of  $\text{Cu}_2\text{O}$  are accumulated on the rGO to form an electron transfer channel. Thus both Ag and rGO are employed to accept the photo-excited electrons from the  $\text{Cu}_2\text{O}$ , which effectively improves the separation rate of  $e^-$  and  $h^+$ . The photo-

excited electrons transferred to the Ag and rGO surfaces can be trapped by the adsorbed  $\text{O}_2$  to form a superoxide anion radicals ( $\cdot\text{O}_2^-$ ), which has strong oxidative properties to degrade the dye molecules. At the same time, the photo-excited  $h^+$  in the VB of the  $\text{Cu}_2\text{O}$  can directly oxidize organic molecules, as shown in Fig. S8.

#### 4. Conclusion

A novel  $\text{Ag-Cu}_2\text{O/rGO}$  heterostructure where octahedral  $\text{Cu}_2\text{O}$  is decorated with dense Ag nanoparticles and is wrapped with rGO nanosheets, has been successfully constructed using a facile route. The  $\text{Ag-Cu}_2\text{O/rGO}$  composite possesses a wide range of light absorption range and low recombination rate of photo-excited carriers. Both the Ag and rGO act as acceptor of photo-excited electrons from  $\text{Cu}_2\text{O}$ , which effectively improves the separation of electron-hole pairs. The surrounding of rGO nanosheets prevents the coarsening of Ag nanoparticles and improves the stability of the octahedral  $\text{Ag-Cu}_2\text{O}$  structure. As a result, the  $\text{Ag-Cu}_2\text{O/rGO}$  photocatalyst exhibits superior photocatalytic activity and stability to the phenol under visible light.

#### Acknowledgements

This work is financially supported by the Zhejiang Provincial Natural Science Foundation of China (No. LR14B060002 and LY18B060005), the Foundation of Zhejiang Educational Committee

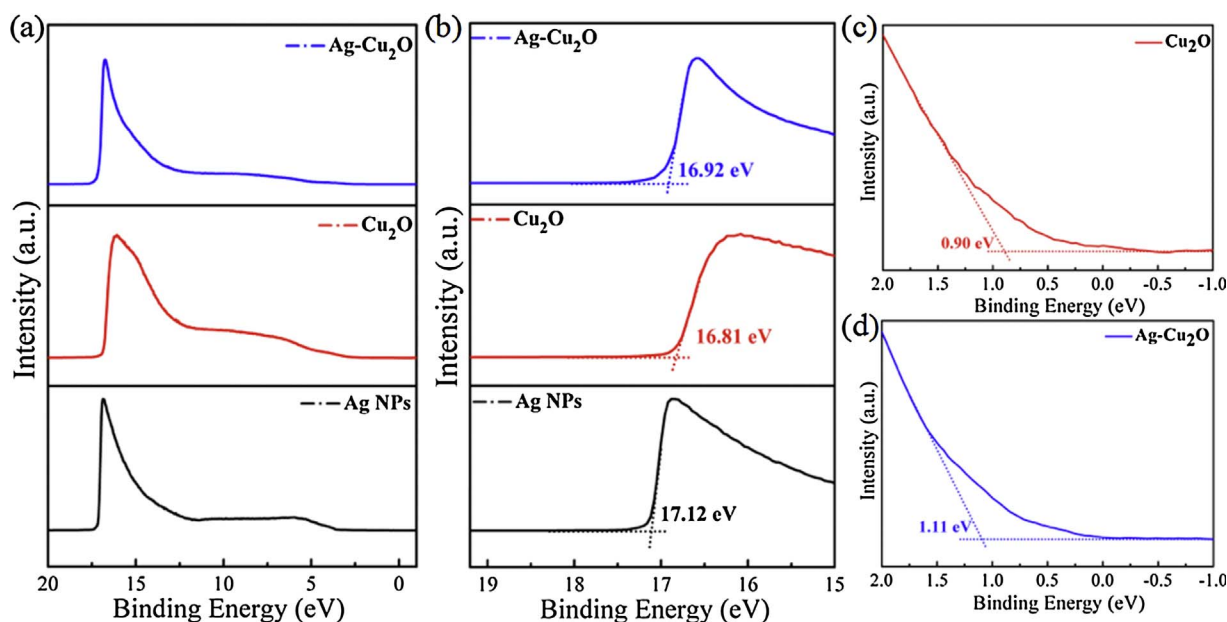


Fig. 17. (a) UPS spectra of the synthesized Ag NPs,  $\text{Cu}_2\text{O}$  and  $\text{Ag-Cu}_2\text{O}$  used for the determination of the VB maximum energies and work function. (b) Expanded UPS spectra. (c) The tangent line of the spectrum onset for  $\text{Cu}_2\text{O}$  and  $\text{Ag-Cu}_2\text{O}$ .



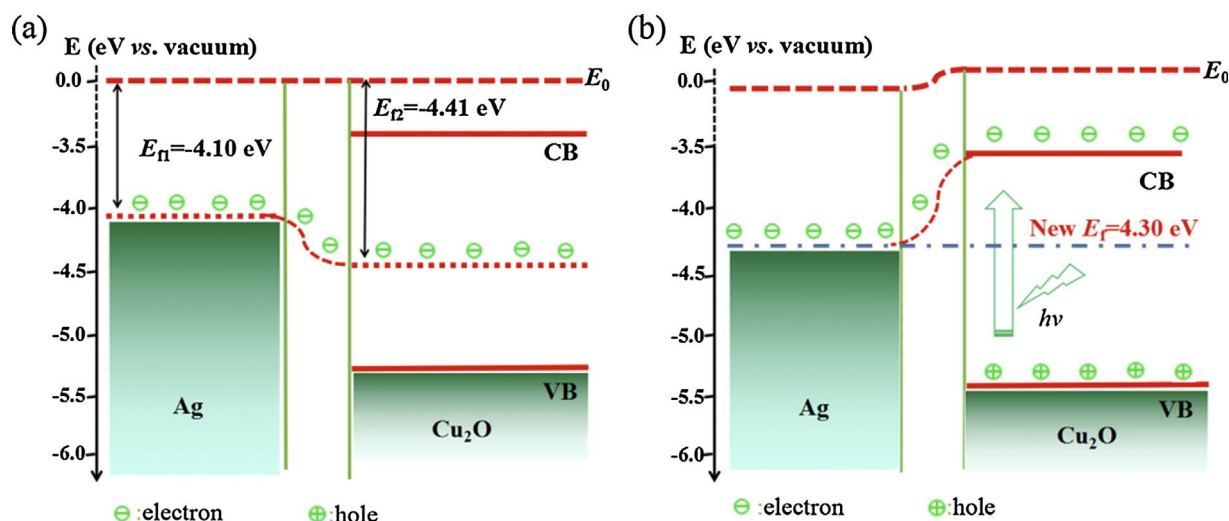


Fig. 18. The band structure of Cu<sub>2</sub>O and Ag junction and Fermi energy level equilibrium without visible light irradiation.

(No. Y201635734).

## Appendix A. Supplementary data

Supplementary data associated with this article can be found, in the online version, at <https://doi.org/10.1016/j.apcatb.2018.01.003>.

## References

- [1] A. Iwase, Y.H. Ng, Y. Ishiguro, A. Kudo, R. Amal, Reduced graphene oxide as a solid-state electron mediator in Z-scheme photocatalytic water splitting under visible light, *J. Am. Chem. Soc.* 133 (2011) 11054–11057.
- [2] G. Tian, H. Fu, L. Jing, B. Xin, K. Pan, Preparation and characterization of stable biphasic TiO<sub>2</sub> photocatalyst with high crystallinity, large surface area, and enhanced photoactivity, *J. Phys. Chem. C* 112 (2008) 3083–3089.
- [3] Y. Lai, M. Meng, Y. Yu, X. Wang, T. Ding, Photoluminescence and photocatalysis of the flower-like nano-ZnO photocatalysts prepared by a facile hydrothermal method with or without ultrasonic assistance, *Appl. Catal. B: Environ.* 105 (2011) 335–345.
- [4] S. Ren, B. Wang, H. Zhang, P. Ding, Q. Wang, Sandwiched ZnO@Au@Cu<sub>2</sub>O nanorod films as efficient visible-light-driven plasmonic photocatalysts, *ACS Appl. Mater. Interfaces* 7 (2015) 4066–4074.
- [5] W. Fan, X. Wang, M. Cui, D. Zhang, Y. Zhang, T. Yu, L. Guo, Differential oxidative stress of octahedral and cubic Cu<sub>2</sub>O micro/nanocrystals to *Daphnia magna*, *Environ. Sci. Technol.* 46 (2012) 10255–10262.
- [6] A. Radi, D. Pradhan, Y. Sohn, K. Leung, Nanoscale shape and size control of cubic, cuboctahedral, and octahedral Cu<sub>2</sub>O core-shell nanoparticles on Si (100) by one-step templateless, capping-agent-free electrodeposition, *ACS Nano* 4 (2010) 1553–1560.
- [7] J. Zhang, C. Zhang, S. Liu, Ammonia-assisted epitaxial assembly of Cu<sub>2</sub>O@Ag yolk-shell and Ag cage, *RSC Adv.* 4 (2014) 21171–21175.
- [8] Y.-C. Pu, H.-Y. Chou, W.-S. Kuo, K.-H. Wei, Y.-J. Hsu, Interfacial charge carrier dynamics of cuprous oxide-reduced graphene oxide (Cu<sub>2</sub>O-rGO) nanoheterostructures and their related visible-light-driven photocatalysis, *Appl. Catal. B: Environ.* 204 (2017) 21–32.
- [9] L. Xu, F. Zhang, X. Song, Z. Yin, Y. Bu, Construction of reduced graphene oxide-supported Ag-Cu<sub>2</sub>O composites with hierarchical structures for enhanced photocatalytic activities and recyclability, *J. Mater. Chem. A* 3 (2015) 5923–5933.
- [10] L. Li, J. Zhang, X. Fu, P. Xiao, M. Zhang, M. Liu, One-pot solid-state reaction approach to synthesize Ag-Cu<sub>2</sub>O/GO ternary nanocomposites with enhanced visible-light-responsive photocatalytic activity, *Int. J. Photoenergy* 2017 (2017).
- [11] D.-F. Zhang, H. Zhang, L. Guo, K. Zheng, X.-D. Han, Z. Zhang, Delicate control of crystallographic facet-oriented Cu<sub>2</sub>O nanocrystals and the correlated adsorption ability, *J. Mater. Chem.* 19 (2009) 5220–5225.
- [12] A. Li, P. Li, J. Hu, W. Zhang, Crystal-facet-controllable synthesis of Cu<sub>2</sub>O microcrystals, shape evolution and their comparative photocatalytic activity, *J. Mater. Sci.: Mater. Electron.* 26 (2015) 5071–5077.
- [13] D.C. Marcano, D.V. Kosynkin, J.M. Berlin, A. Sinitskii, Z. Sun, A. Slesarev, L.B. Alemany, W. Lu, J.M. Tour, Improved synthesis of graphene oxide, *ACS Nano* 4 (2010).
- [14] Y.-G. Zhang, L.-L. Ma, J.-L. Li, Y. Yu, In situ Fenton reagent generated from TiO<sub>2</sub>/Cu<sub>2</sub>O composite film: a new way to utilize TiO<sub>2</sub> under visible light irradiation, *Environ. Sci. Technol.* 41 (2007) 6264–6269.
- [15] Y. Li, W. Zhang, X. Shen, P. Peng, L. Xiong, Y. Yu, Octahedral Cu<sub>2</sub>O-modified TiO<sub>2</sub> nanotube arrays for efficient photocatalytic reduction of CO<sub>2</sub>, *Chin. J. Catal.* 36 (2015) 2229–2236.
- [16] Y. Ding, P. Zhang, Q. Zhuo, H. Ren, Z. Yang, Y. Jiang, A green approach to the synthesis of reduced graphene oxide nanosheets under UV irradiation, *Nanotechnology* 22 (2011) 215601.
- [17] S. Dutta, K. Das, K. Chakrabarti, D. Jana, S. De, S. De, Highly efficient photocatalytic activity of CuO quantum dot decorated rGO nanocomposites, *J. Phys. D: Appl. Phys.* 49 (2016) 315107.
- [18] I. Roy, A. Bhattacharyya, G. Sarkar, N.R. Saha, D. Rana, P.P. Ghosh, M. Palit, A.R. Das, D. Chattopadhyay, In situ synthesis of a reduced graphene oxide/cuprous oxide nanocomposite: a reusable catalyst, *RSC Adv.* 4 (2014) 52044–52052.
- [19] L. Zhao, C. Hong, L. Lin, H. Wu, Y. Su, X. Zhang, A. Liu, Controllable nanoscale engineering of vertically aligned MoS<sub>2</sub> ultrathin nanosheets by nitrogen doping of 3D graphene hydrogel for improved electrocatalytic hydrogen evolution, *Carbon* 116 (2017) 223–231.
- [20] Y. Fan, W. Ma, D. Han, S. Gan, X. Dong, L. Niu, Convenient recycling of 3D AgX/graphene aerogels (X = Br, Cl) for efficient photocatalytic degradation of water pollutants, *Adv. Mater.* 27 (2015) 3767–3773.
- [21] J. Yang, Z. Li, C. Zhao, Y. Wang, X. Liu, Facile synthesis of Ag-Cu<sub>2</sub>O composites with enhanced photocatalytic activity, *Mater. Res. Bull.* 60 (2014) 530–536.
- [22] J. Wang, S. Liang, L. Ma, S. Ding, X. Yu, L. Zhou, Q. Wang, One-pot synthesis of CdS-reduced graphene oxide 3D composites with enhanced photocatalytic properties, *CrystEngComm* 16 (2014) 399–405.
- [23] Q. Li, B. Guo, J. Yu, J. Ran, B. Zhang, H. Yan, J.R. Gong, Highly efficient visible-light-driven photocatalytic hydrogen production of CdS-cluster-decorated graphene nanosheets, *J. Am. Chem. Soc.* 133 (2011) 10878–10884.
- [24] Q.-P. Luo, X.-Y. Yu, B.-X. Lei, H.-Y. Chen, D.-B. Kuang, C.-Y. Su, Reduced graphene oxide-hierarchical ZnO hollow sphere composites with enhanced photocurrent and photocatalytic activity, *J. Phys. Chem. C* 116 (2012) 8111–8117.
- [25] X. Cao, G. Tian, Y. Chen, J. Zhou, W. Zhou, C. Tian, H. Fu, Hierarchical composites of TiO<sub>2</sub> nanowire arrays on reduced graphene oxide nanosheets with enhanced photocatalytic hydrogen evolution performance, *J. Mater. Chem. A* 2 (2014) 4366–4374.
- [26] Y. Chen, G. Tian, Z. Ren, K. Pan, Y. Shi, J. Wang, H. Fu, Hierarchical core-shell carbon nanofiber@ZnIn<sub>2</sub>S<sub>4</sub> composites for enhanced hydrogen evolution performance, *ACS Appl. Mater. Interfaces* 6 (2014) 13841–13849.
- [27] L. Yu, G. Li, X. Zhang, X. Ba, G. Shi, Y. Li, P.K. Wong, J.C. Yu, Y. Yu, Enhanced activity and stability of carbon-decorated cuprous oxide mesoporous nanorods for CO<sub>2</sub> reduction in artificial photosynthesis, *ACS Catal.* 6 (2016) 6444–6454.
- [28] B. Luo, X. Li, X. Li, L. Xue, S. Li, X. Li, Copper nanocubes and nanostructured cuprous oxide prepared by surfactant-assisted electrochemical deposition, *CrystEngComm* 15 (2013) 5654–5659.
- [29] S. Poulston, P. Parlett, P. Stone, M. Bowker, Surface oxidation and reduction of CuO and Cu<sub>2</sub>O studied using XPS and XAES, *Surf. Interface Anal.* 24 (1996) 811–820.
- [30] M. Fantauzzi, D. Atzei, B. Elsener, P. Lattanzi, A. Rossi, XPS and XAES analysis of copper, arsenic and sulfur chemical state in enargites, *Surf. Interface Anal.* 38 (2006) 922–930.
- [31] D. Lin, H. Wu, R. Zhang, W. Pan, Enhanced photocatalysis of electrospun Ag-ZnO heterostructured nanofibers, *Chem. Mater.* 21 (2009) 3479–3484.
- [32] Q. Deng, H. Tang, G. Liu, X. Song, G. Xu, Q. Li, D.H. Ng, G. Wang, The fabrication and photocatalytic performances of flower-like Ag nanoparticles/ZnO nanosheets-assembled microspheres, *Appl. Surf. Sci.* 331 (2015) 50–57.
- [33] Y. Zheng, L. Zheng, Y. Zhan, X. Lin, Q. Zheng, K. Wei, Ag/ZnO heterostructure nanocrystals: synthesis, characterization, and photocatalysis, *Inorg. Chem.* 46 (2007) 6980–6986.
- [34] G. Wang, X. Shen, J. Yao, J. Park, Graphene nanosheets for enhanced lithium storage in lithium ion batteries, *Carbon* 47 (2009) 2049–2053.
- [35] M.H. Huang, S. Rej, S.-C. Hsu, Facet-dependent properties of polyhedral nanocrystals, *Chem. Commun.* 50 (2014) 1634–1644.
- [36] H. Wang, L. Zhang, Z. Chen, J. Hu, S. Li, Z. Wang, J. Liu, X. Wang, Semiconductor heterojunction photocatalysts: design, construction, and photocatalytic

- performances, *Chem. Soc. Rev.* 43 (2014) 5234–5244.
- [37] X. An, K. Li, J. Tang, Cu<sub>2</sub>O/reduced graphene oxide composites for the photocatalytic conversion of CO<sub>2</sub>, *ChemSusChem* 7 (2014) 1086–1093.
- [38] Y.-C. Pu, Y.-C. Chen, Y.-J. Hsu, Au-decorated Na<sub>x</sub>H<sub>2</sub>-xTi<sub>3</sub>O<sub>7</sub> nanobelts exhibiting remarkable photocatalytic properties under visible-light illumination, *Appl. Catal. B: Environ.* 97 (2010) 389–397.
- [39] J. Li, L. Sun, Y. Yan, Z. Zhu, One-step in-situ fabrication of silver-modified Cu<sub>2</sub>O crystals with enhanced visible photocatalytic activity, *Micro Nano Lett.* 11 (2016) 363–365.
- [40] W. Lu, S. Gao, J. Wang, One-pot synthesis of Ag/ZnO self-assembled 3D hollow microspheres with enhanced photocatalytic performance, *J. Phys. Chem. C* 112 (2008).
- [41] H. Zhang, L. Zhao, F. Geng, L.-H. Guo, B. Wan, Y. Yang, Carbon dots decorated graphitic carbon nitride as an efficient metal-free photocatalyst for phenol degradation, *Appl. Catal. B: Environ.* 180 (2016) 656–662.
- [42] Y. Qu, X. Duan, Progress, challenge and perspective of heterogeneous photocatalysts, *Chem. Soc. Rev.* 42 (2013) 2568–2580.
- [43] Q. Xiang, J. Yu, M. Jaroniec, Enhanced photocatalytic H<sub>2</sub>-production activity of graphene-modified titania nanosheets, *Nanoscale* 3 (2011) 3670–3678.
- [44] F. Liang, Y. Zhu, Enhancement of mineralization ability for phenol via synergetic effect of photoelectrocatalysis of gC<sub>3</sub>N<sub>4</sub> film, *Appl. Catal. B: Environ.* 180 (2016) 324–329.
- [45] Y. Li, Y. Jiang, Z. Ruan, K. Lin, Z. Yu, Z. Zheng, X. Xu, Y. Yuan, Simulation-guided synthesis of graphitic carbon nitride beads with 3D interconnected and continuous meso/macropore channels for enhanced light absorption and photo-catalytic performance, *J. Mater. Chem. A* 5 (40) (2017) 21300–21312.
- [46] K. Wismulek, J. Sar, P. Osewski, K. Orlinski, K. Kolodziejek, A. Tenczek-Zajac, M. Radecka, D.A. Pawlak, A SrTiO<sub>3</sub>-TiO<sub>2</sub> eutectic composite as a stable photoanode material for photoelectrochemical hydrogen production, *Appl. Catal. B: Environ.* 206 (2017) 538–546.
- [47] H. Zhang, L.-H. Guo, L. Zhao, B. Wan, Y. Yang, Switching oxygen reduction pathway by exfoliating graphitic carbon nitride for enhanced photocatalytic phenol degradation, *J. Phys. Chem. Lett.* 6 (2015) 958–963.
- [48] J.-N. Nian, C.-C. Tsai, P.-C. Lin, H. Teng, Elucidating the conductivity-type transition mechanism of p-type Cu<sub>2</sub>O films from electrodeposition, *J. Electrochem. Soc.* 156 (2009) H567–H573.
- [49] S. Upadhyay, D. Sharma, N. Singh, V.R. Satsangi, R. Shrivastav, U.V. Waghmare, S. Dass, Experimental and first-principles theoretical studies on Ag-doped cuprous oxide as photocathode in photoelectrochemical splitting of water, *J. Mater. Sci.* 49 (2013) 868–876.
- [50] T.-F. Yeh, S.-J. Chen, C.-S. Yeh, H. Teng, Tuning the electronic structure of graphite oxide through ammonia treatment for photocatalytic generation of H<sub>2</sub> and O<sub>2</sub> from water splitting, *J. Phys. Chem. C* 117 (2013) 6516–6524.
- [51] M. Li, L. Zhang, X. Fan, Y. Zhou, M. Wu, J. Shi, Highly selective CO<sub>2</sub> photoreduction to CO over gC<sub>3</sub>N<sub>4</sub>/Bi<sub>2</sub>WO<sub>6</sub> composites under visible light, *J. Mater. Chem. A* 3 (2015) 5189–5196.
- [52] Y.-H. Chiu, Y.-J. Hsu, Au@Cu<sub>7</sub>S<sub>4</sub> yolk@shell nanocrystal-decorated TiO<sub>2</sub> nanowires as an all-day-active photocatalyst for environmental purification, *Nano Energy* 31 (2017) 286–295.
- [53] P. Christopher, D.B. Ingram, S. Linic, Enhancing photochemical activity of semiconductor nanoparticles with optically active Ag nanostructures: photochemistry mediated by Ag surface plasmons, *J. Phys. Chem. C* 114 (2010) 9173–9177.
- [54] J. Zhang, Z. Xiong, X.S. Zhao, Graphene-metal-oxide composites for the degradation of dyes under visible light irradiation, *J. Mater. Chem.* 21 (2011) 3634–3640.
- [55] S.K. Bhunia, N.R. Jana, Reduced graphene oxide-silver nanoparticle composite as visible light photocatalyst for degradation of colorless endocrine disruptors, *ACS Appl. Mater. Interfaces* 6 (2014) 20085–20092.